Selectively Strong Coupling of MoS$_2$ Excitons to a Metamaterial at Room Temperature

Harshavardhan R. Kalluru[*] and Jaydeep K. Basu

Department of Physics, Indian Institute of Science, Bangalore 560012, India

Light emitters in the vicinity of a hyperbolic metamaterial (HMM) show a range of quantum optical phenomena from spontaneous decay-rate enhancement to strong coupling. In this study, we integrate a monolayer molybdenum disulfide (MoS$_2$) emitter in the near-field region of the HMM. The MoS$_2$ monolayer has *A* and *B* excitons, which emit in the red region of the visible spectrum. We find that the *B* excitons couple to the HMM differently compared to *A* excitons. The fabricated HMM transforms to a hyperbolic dispersive medium at 2.14 eV, from an elliptical dispersive medium. The selective coupling of *B* excitons to the HMM modes is attributed to the inbuilt field gradient of the transition. The *B* exciton energy lies close to the transition point of the HMM, relative to the *A* exciton. So, the HMM modes couple more to the *B* excitons and the metamaterial functions as a selective coupler. The coupling strength calculations show that coupling is 2.5 times stronger for *B* excitons relative to *A* excitons. High near field of HMM, large magnitude, and the in-plane transition dipole moment of MoS$_2$ excitons, result in strong coupling of *B* excitons and formation of hybrid light-matter states. The measured differential reflection and photoluminescence spectra indicate the presence of hybrid light-matter states, i.e., exciton polaritons. Rabi splitting of 143.5 meV $\pm$ 14.4 meV at room temperature is observed. The low-temperature photoluminescence measurement shows mode anticrossing, which is a characteristic feature of hybrid states. Our results show that the HMM works as an energy-selective coupler for multiexcitonic systems as MoS$_2$.

I. INTRODUCTION

The hyperbolic metamaterial (HMM) undergoes an optical topological transition (OTT) and the isofrequency surface of HMM changes from an ellipsoid to a hyperboloid at the transition point. The volume under the isofrequency surface is the photonic density of states (PDOS). The hyperbolic isofrequency surface is nonintegrable. As a consequence of OTT, the PDOS of HMM diverges [1]. Due to diverging PDOS and the nature of propagating hyperbolic modes [2], the HMM system has been studied extensively for controlling light-matter interaction.

The evanescent modes with large wave vector propagating through the volume of HMM enable superresolution imaging of subdiffraction size objects in far field [3,4]. HMM has been used to sense picomolar concentrations of biomolecules [5,6]. The interface between HMM and a photonic crystal as a Bragg mirror, can support optical Tamm states [7]. The optical Tamm state wave vectors lie within the light cone and can be directly excited by incident light beam [8]. This has applications in broadband absorbing materials, optical filters [9], and photovoltaic devices [10].

It has been demonstrated that a collection of emitters on hyperbolic materials show strong coupling near the OTT set-in point [11]. Modification of spontaneous emission rate of dye molecules, [12] rare earth ions [13], and strong coupling of semiconductor quantum dots [14] in the vicinity of HMM is reported. The transition energy can be tuned by changing the fabrication parameters.

Monolayer molybdenum disulphide (MoS$_2$) is the light emitter used for coupling with the HMM. MoS$_2$ belongs to a class of layered van der Waals materials called transition-metal dichalcogenides (TMDCs). These materials can be exfoliated mechanically to the monolayer limit. The monolayer MoS$_2$ is a direct band-gap semiconductor [15]. It has applications in light-emitting devices [16], optical valley control devices [17], energy-storage systems [18], and piezoelectric [19] devices. A monolayer MoS$_2$ system has neutral excitons, charged excitons, localized excitons, and dark excitons [20].

The orientation of transition dipole moment (TDM) of emitters relative to the metal-dielectric interface of the HMM determines the PDOS experienced by the emitters [21] and the efficiency of coupling [22]. If the TDM is oriented normal to metal-dielectric interface of the HMM, the coupling is optimum to the plasmonic modes.

Due to the in-plane orientation [23] of TDM, the monolayer MoS$_2$ excitons are well suited for coupling to

*kallurureddy@iisc.ac.in

silver-nanowire-based HMM. The maximum field of the TDM is normal to the plane of the monolayer. So the PL emission of the MoS$_2$ monolayer is ideal for driving the longitudinal plasma oscillations in silver nanowires of the HMM. The high TDM magnitude [24] of TMDC excitons approximately 50 debye is also an additive factor for optimal coupling.

Strong coupling [25] of emitters and HMM is observed, when the coupling strength dominates the emitter spontaneous decay rate and HMM losses. Strong coupling results in Rabi splitting in the frequency domain. The magnitude and orientation of the emitter TDM (μ) determines the energy decay rate into vacuum and HMM. The HMM PDOS determines the field strength (E). The PDOS is highest near OTT set-in point and gradually decreases as the exciton emission peak moves away from the transition point. So both factors determine the coupling coefficient g of a single emitter, given by [26]

$$g = \frac{\mu E}{\hbar}. \tag{1}$$

We show that the MoS$_2$ B excitons are strongly coupled to HMM and the Rabi splitting is 143.5 meV $\pm$ 14.4 meV at room temperature. A similar value of Rabi splitting (101 meV) is reported for WS$_2$ coupled metallic nanostructures [27]. Rabi splitting of 58 meV at 77 K is reported for the MoS$_2$ monolayer coupled plasmonic lattice system [28]. The lithographic processes used for fabricating nanoscale plasmonic systems are expensive. Silver-nanowire-based HMM used in this study is made through standard electrochemical processes of the aluminum metal-finishing industry [29], which is an inexpensive alternative. The fabricated HMM is an industrially scalable coupler, which can selectively strong couple MoS$_2$ excitons at room temperature.

II. EXPERIMENTAL METHODS

The HMM is fabricated on a glass substrate for room-temperature measurements. Exfoliated MoS$_2$ monolayer is transferred onto the HMM with a 10-nm polymer spacer. The Raman and white-light reflection spectra are collected with a confocal microscope (Witec alpha 300). A 532-nm laser diode is used for Raman-spectra measurement and the spectra are collected with 100$\times$ magnification and 0.9 NA bright-field objective. The signal from the sample is relayed to a grating coupled Peltier cooled CCD. For low-temperature photoluminescence measurement the sample is fabricated on a silicon (with 300-nm oxide) substrate. The sample is placed in a closed cycle cryostat (Montana), which is capable of reaching until 6 K. The cryostat is placed directly under a microscope system (Horiba labram) for PL measurement in reflection mode. The PL spectra are excited with a 532-nm frequency-doubled Nd:YAG laser and are collected with a 50$\times$
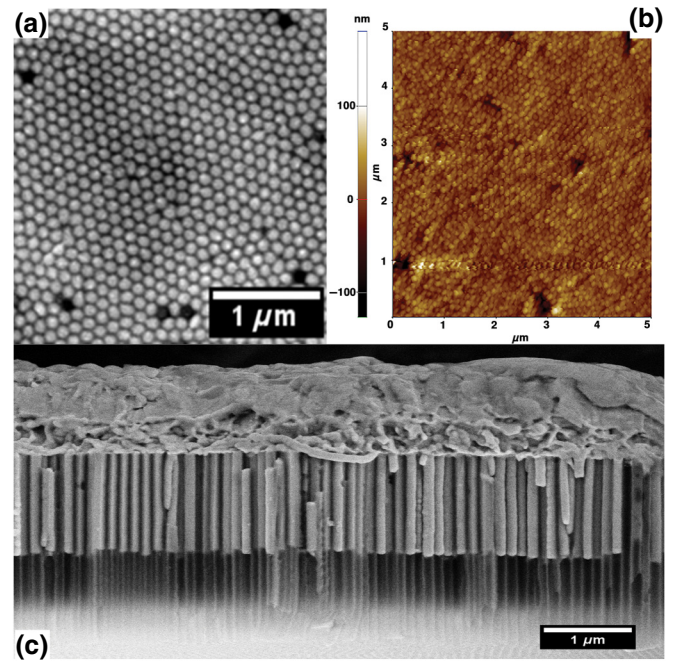

FIG. 1. Characterization of fabricated hyperbolic metamaterial. (a) The SEM image of the region etched with a focused ion beam (FIB). (b) The AFM image of 5 $\times$ 5 μm^2 region of the roughened side of the HMM with a 10-nm spacer. (c) The cross-section SEM image of silver nanowires grown in an aluminum oxide template.

magnification and 0.5-NA objective and relayed onto a grating coupled Peltier cooled CCD.

III. RESULTS AND DISCUSSION

A. HYPERBOLIC METAMATERIAL

The HMM is fabricated as per an earlier work from our group [30], by growing silver nanowires in a porous aluminum oxide film, through electrochemical deposition. (see S1 within the Supplemental Material) [31] The HMM is characterised by scanning electron microscopy (SEM) and atomic force microscopy (AFM), as shown in Fig. 1. The metamaterial undergoes OTT and transforms from a lossy dielectric medium to a hyperbolic dispersive medium. The transition shown in Fig. 2(a), is calculated according to effective-medium-theory (EMT) approximation [32] of the HMM, with silver metal filling fraction 0.15. The absorption coefficient of a system is directly proportional to differential reflectivity (see S4 within the Supplemental Material) [31]. The unpolarized white-light differential reflection (DR) spectra of the HMM are measured and shown in Fig. 2(b). The OTT of the HMM is seen as a smooth transition [33], which is attributed to losses in the HMM.

The HMM DR spectra has a broad feature between 1.9 and 2.1 eV. To find out the critical point, where transition
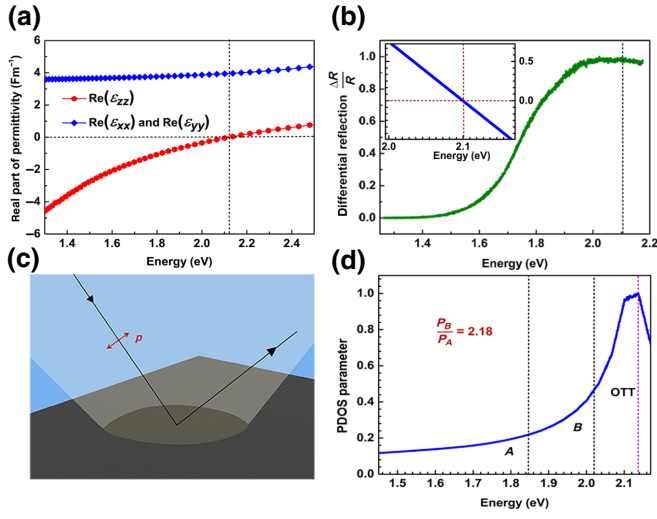
FIG. 2. (a) The calculated OTT of HMM. (b) The measured DR spectra of HMM and the inlay shows the first-order derivative of DR spectra. (c) Schematic for HMM white-light reflection. (d) The calculated PDOS parameter (P) for the HMM. The lines indicate the positions of A and B excitons.

occurs, the first-order derivative of measured DR is shown in the inset of Fig. 2(b). The critical point is at 2.1003 eV ± 0.8 meV, which is in good agreement with the calculated EMT transition point 2.1378 eV. So the EMT description of HMM is accurate. From a theoretical perspective, the light free-space wavelength (in this paper $\lambda_o > 500$ nm) is much larger than the period (133 nm) of the unit cell. So the HMM should behave as an effective medium, which is what we see in DR spectra. The monolayer MoS₂ has three luminescent excitons [34,35] namely, A (about 1.8 eV), B (at 2.0 eV), and C (at 2.8 eV). The C exciton is not useful for coupling, as it is in elliptical dispersive region of HMM.

B. COUPLING STRENGTH CALCULATIONS

The selective strong coupling of B excitons to HMM can be understood by considering the difference in PDOS at the exciton positions and the relative oscillator strength of B and A excitons. The PDOS parameter (P) of a lossy hyperbolic half space [36] is calculated from reported values of refractive indices and extinction coefficients of silver and alumina (see S10 within the Supplemental Material) [31].

$$P = \frac{2\sqrt{\epsilon_{xx}|\epsilon_{zz}|}}{(1 + \epsilon_{xx}|\epsilon_{zz}|)} + \epsilon'' \frac{(\epsilon_{xx} - |\epsilon_{zz}|)}{(1 + \epsilon_{xx}|\epsilon_{zz}|)^2}. \quad (2)$$

The measured absorption data is incorporated in the PDOS calculation as the loss factor (ϵ''). Here the Z axis is the growth direction of nanowires and ϵ_{xx}, ϵ_{zz} are effective permittivity values along X and Z axes. The calculated PDOS is shown in Fig. 2(d). The PDOS is directly proportional to the electric field (E) [37]. So the ratio of HMM electric

field at B (2.0222 eV) to A (1.8463 eV) exciton position is given by

$$\frac{P_B}{P_A} = \frac{E_B}{E_A} = 2.18. \quad (3)$$

The oscillator strength (μ^2) of an exciton [38] is directly proportional to the absorption coefficient (α). The relative oscillator strength of B to A excitons is extracted from measured monolayer MoS₂ DR spectra.

$$\frac{\mu_B^2}{\mu_A^2} = \frac{\alpha_B}{\alpha_A} = 1.49. \quad (4)$$

The exciton population (N) is directly proportional to the PL intensity of MoS₂ excitons at room temperature (see S5 within the Supplemental Material) [31]. The ratio turns out as

$$\frac{N_B}{N_A} = \frac{I_B}{I_A} = 0.88. \quad (5)$$

The coupling coefficient (g) for a population of N excitons [39,40] is given by $\hbar g = \sqrt{N}\mu E$, where μ is the excitonic transition dipole moment and E is the HMM electric field. The ratio of coupling coefficients is calculated by combining Eqs. (3), (4), and (5).

$$\frac{g_B}{g_A} = \sqrt{\frac{N_B}{N_A}} \frac{\mu_B P_B}{\mu_A P_A} = 2.50. \quad (6)$$

The coupling at the B exciton is 2.5 times larger than the coupling at the A exciton. So, the HMM can act as a selective coupler for MoS₂ excitons.

C. COUPLED MoS₂-HMM SYSTEM

Bulk MoS₂ pieces are mechanically exfoliated using scotch tape until the monolayer limit is reached. The monolayer is transferred [41,42] onto the HMM, by dry visco-elastic gel stamping (see S2 and S3 within the Supplemental Material) [31].

The measured DR spectra for the HMM, monolayer MoS₂ system on glass and monolayer MoS₂ on the HMM are plotted in Fig. 3(b). The DR spectra of MoS₂ monolayer on glass has two peaks at 1.8463 eV ± 0.8 meV and 2.0222 eV ± 0.8 meV, corresponding to A and B excitons, respectively. An extra peak at 1.9280 eV ± 0.8 meV is observed between the positions of A and B excitons, in DR spectra of the coupled monolayer MoS₂-HMM system.

The measured PL spectra for monolayer MoS₂ on the HMM and the monolayer MoS₂ system on silicon with varying temperature are shown in Figs. 4(a) and 4(b), respectively. The room-temperature (289-K) PL spectral envelope of monolayer MoS₂ on the HMM is modified
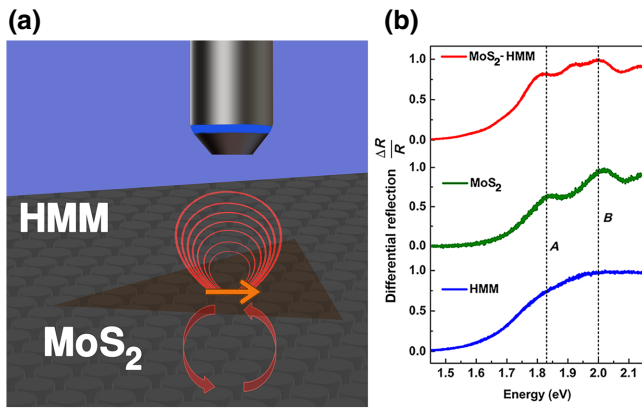
FIG. 3. (a) Configuration for coupling MoS₂ excitonic transition dipole moment to the HMM. (b) The DR spectra of HMM, monolayer MoS₂, and coupled monolayer MoS₂-HMM system, respectively.

and an extra peak (ω_-) appears at 1.8955 eV $\pm$ 7.2 meV. So another peak is observed in both DR (absorption) and PL (emission) spectra, which confirms strong coupling [43]. Only three spectra at different temperatures are shown for brevity (see S6 within the Supplemental Material) [31].

The MoS₂ monolayer Debye temperature [44] is 262 K, which is close to room temperature. So the PL peak position is sensitive to cooling, as PL is a band-edge emission process. The MoS₂ A and B exciton PL peak positions blue shift on cooling to cryogenic temperatures, [45] whereas the plasmonic modes are temperature insensitive. Lowering temperature can detune [46] the PL spectra and is used

to visualize anticrossing [47] behavior of the MoS₂-HMM coupled system.

The losses are always significant in a plasmonic system as HMM due to the scattering [48] of electrons by phonons, electron-electron scattering, and direct scattering by surface plasmon polaritons (SPPs). When cooled down to cryogenic temperatures, phonon-electron scattering reduces drastically, which results in longer [49] propagation lengths of SPPs. Essentially a fraction of HMM losses can be minimized, by cooling the system, which is an added advantage of low-temperature PL measurement. So, temperature-dependent PL detuning measurement can help to understand whether the A or B exciton is strongly coupled to the HMM. Mode anticrossing is observed for strongly coupled polariton modes [50,51]. While detuning, one polariton mode moves towards the exciton line and the other polariton mode moves away from the exciton line [52,53].

We focus on PL features in the region from 1.8 to 2.1 eV in this paper, as the features related to A and B excitons appear in it. The monolayer MoS₂ PL peak position is strongly dependent [54] on the substrate and dielectric environment. The refractive index of the HMM also changes with temperature. To make sense of the low-temperature PL data, two control measurements (see S7 within the Supplemental Material) [31] are done, to account for the temperature-dependent refractive index of the environment. Rhodamine B dye molecule PL peak position is independent [55] of temperature. So for control measurements, Rhodamine B dye solution is drop casted on to both the HMM and silicon with a spacer. Monolayer MoS₂ is transferred onto silicon with a spacer as a reference sample for exciton peak blue shift.

The collected PL spectra, of all the samples are fitted with Lorentzian function (see S8 within the Supplemental Material) [31] and the corresponding peak positions are obtained. The MoS₂ PL peak shifts observed on the HMM and silicon sample are corrected with respective control samples with Rhodamine B dye. The measured temperature points range from 6 ± 0.05 K to room temperature. The B exciton peaks for MoS₂ on silicon are fitted with a line. The corrected peak positions are shown in Figs. 4(c) and 4(d). To visualize the evolution of peaks in Fig. 4(c), the energies of the peaks adjacent to the B exciton are subtracted with the MoS₂ B exciton energy and are shown in Fig. 5. With lowering temperature, the subtracted upper polariton branch $[\omega_+ - \omega_B]$ moves towards the B exciton line and the subtracted lower polariton branch $[\omega_- - \omega_B]$ moves away from the B exciton line. The anticrossing of modes, confirms that the B excitons of monolayer MoS₂ are strongly coupled with HMM plasmonic modes and form exciton plasmon polaritons. The A excitons peaks on the HMM and on control silicon lie within the error bar of 14.4 meV (see S9 within the Supplemental Material) [31]. Anticrossing is not observed for A excitons. So they are not
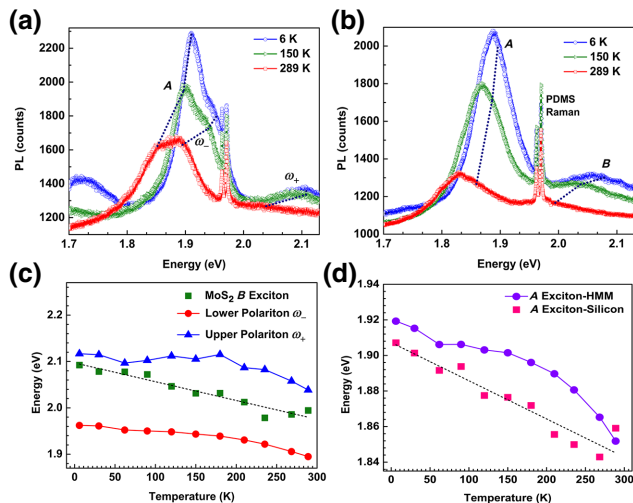

FIG. 4. (a) Measured temperature-dependent PL of monolayer MoS₂ coupled to HMM. (b) Temperature-dependent PL of monolayer MoS₂ on silicon substrate. (c),(d) Evolution of PL peak features of both monolayer MoS₂ on silicon and monolayer MoS₂ coupled to the HMM with lowering temperature.
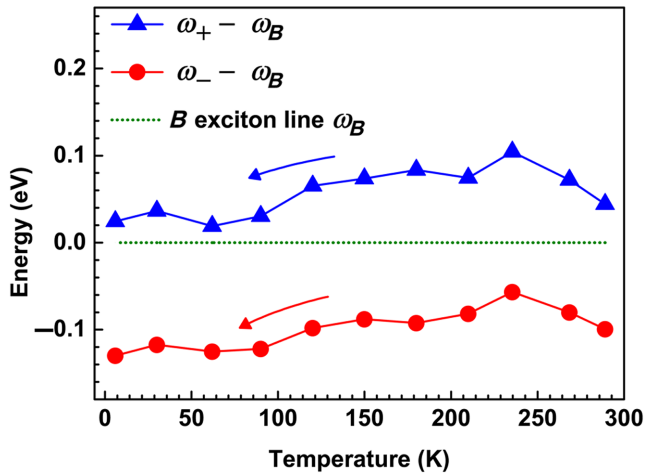
FIG. 5. Evolution of peaks with respect to the B exciton line with lowering temperature.

strongly coupled with HMM modes. The B excitons are selectively strong coupled to the HMM modes. The separation between the upper and lower polariton branches is considered as Rabi splitting. From Fig. 4(c), its value turns out as 143.5 meV $\pm$ 14.4 meV at room temperature.

We show, due to the inbuilt field gradient of metamaterial, the nature of coupling is different for B and A excitons. The B excitons are strongly coupled to metamaterial at room temperature.

In principle, the OTT of HMM can be tuned to coincide with A exciton of monolayer MoS$_2$, by modifying the silver-metal filling fraction to $f = 0.12$ (see S10 within the Supplemental Material) [31]. At energies higher than the OTT set-in point, the HMM behaves as a dielectric medium. In this case only A excitons will interact directly with HMM modes.

Apart from the coupling strength considerations, the monolayer MoS$_2$ is a direct band-gap semiconductor. So, the PL emission intensity linearly varies with the incident laser beam power [56]. The intensity of polaritons will also vary with incident laser power.

If the coupled MoS$_2$-HMM system is excited by a laser diode, then by changing the diode current, the incident beam power can be changed. This in turn will change the intensity of polaritons. So by coding a signal onto the laser diode current source, the signal will be coded into the laser beam, which in turn modulates the polariton intensity. The coupled MoS$_2$-HMM system is industrially scalable and inexpensive, so it has potential for application as an encoder in optical information systems.

IV. DISCUSSION

In order to incorporate Rabi splitting into the mode information of the system, the plasmonic mode of HMM and the B exciton of MoS$_2$ can be modeled as a pair of coupled oscillators.

$$\omega_{\pm} = \omega_B - \frac{i}{2}(\gamma_B + \kappa) \pm \sqrt{g_B^2 - \left(\frac{\gamma_B - \kappa}{2}\right)^2}. \quad (7)$$

Under the coupled oscillator model [11,39], the upper and lower polariton branches can be calculated from Eq. (7). Here g_B and γ_B are the coupling coefficient and vacuum decay rate of B excitons. The HMM loss rate is represented by κ. The physical quantities g_B, γ_B, and κ vary with temperature.

The calculated polariton branches can be incorporated into the response of the coupled system and the Rabi splitting in reflection spectra can be obtained using the coupled oscillator model.

The main challenge to use this approach for the coupled MoS$_2$-HMM system, is to obtain an experimental estimate of the HMM loss rate (κ). The quality factor (Q) [57] of a plasmonic mode central frequency (ω) is given by $Q = \omega/\kappa = \omega/\Delta\omega$. From the white-light reflection spectra (DR), the ratio between the mode central frequency (ω) to the line width ($\Delta\omega$) is considered as the quality factor. From the DR spectra in Fig. 2(b), it can be seen that the HMM has a set-in point at 2.14 eV (visible red region) and extends beyond the near infrared region. So the quality factor cannot be estimated from DR spectra.

The Rabi splitting (Ω) is observed in spectra, the condition for resolving splitting is $\Omega \geq \hbar\gamma_B + \hbar\kappa/2$. This condition sets an upper limit for loss rate. At room temperature, the Rabi splitting is 143.5 meV. So the upper limit for the loss rate is $(2\Omega/\hbar) = 4.36 \times 10^{14}$ Hz, which corresponds to a minimum of 2.3-fs decay time. So the detector resolution to observe the losses in time domain has to be at least 2.3 fs, which is beyond resolution of our instrumental facilities (30 ps).

V. CONCLUSION

The coupled MoS$_2$-HMM system is characterized with differential reflection and temperature-dependent photoluminescence measurements. The mode anticrossing confirms that the B excitons of monolayer MoS$_2$ are strongly coupled to HMM. At room temperature, the measured Rabi splitting is 143.5 meV $\pm$ 14.4 meV. We show that the metamaterial functions as an energy-selective coupler for MoS$_2$ A and B excitons. The relative coupling strength is 2.50 for B to A excitons.

ACKNOWLEDGMENTS

[1] Z. Jacob, J.-Y. Kim, G. V. Naik, A. Boltasseva, E. E. Narimanov, and V. M. Shalaev, Engineering photonic density of states using metamaterials, Appl. Phys. B **100,** 215 (2010).

[2] J. Yao, Z. Liu, Y. Liu, Y. Wang, C. Sun, G. Bartal, A. M. Stacy, and X. Zhang, Optical negative refraction in bulk metamaterials of nanowires, Science **321,** 930 (2008).

[3] Z. Liu, H. Lee, Y. Xiong, C. Sun, and X. Zhang, Far-field optical hyperlens magnifying sub-diffraction-limited objects, Science **315,** 1686 (2007).

[4] B. D. F. Casse, W. T. Lu, Y. J. Huang, E. Gultepe, L. Menon, and S. Sridhar, Super-resolution imaging using a three-dimensional metamaterials nanolens, Appl. Phys. Lett. **96,** 023114 (2010).

[5] A. V. Kabashin, P. Evans, S. Pastkovsky, W. Hendren, G. A. Wurtz, R. Atkinson, R. Pollard, V. A. Podolskiy, and A. V. Zayats, Plasmonic nanorod metamaterials for biosensing, Nat. Mater. **8,** 867 (2009).

[6] K. Sreekanth, Y. Alapan, M. ElKabbash, E. Ilker, M. Hinczewski, U. A. Gurkan, A. D. Luca, and G. Strangi, Extreme sensitivity biosensing platform based on hyperbolic metamaterials, Nat. Mater. **15,** 621 (2016).

[7] R. G. Bikbaev, S. Y. Vetrov, and I. V. Timofeev, Hyperbolic metamaterial for the Tamm plasmon polariton application, J. Opt. Soc. Am. B **37,** 2215 (2020).

[8] M. Kaliteevski, I. Iorsh, S. Brand, R. A. Abram, J. M. Chamberlain, A. V. Kavokin, and I. A. Shelykh, Tamm plasmon-polaritons: Possible electromagnetic states at the interface of a metal and a dielectric Bragg mirror, Phys. Rev. B **76,** 165415 (2007).

[9] F. Wu, K. Lyu, S. Hu, M. Yao, and S. Xiao, Ultra-large omnidirectional photonic band gaps in one-dimensional ternary photonic crystals composed of plasma, dielectric and hyperbolic metamaterial, Opt. Mater. **111,** 110680 (2021).

[10] F. Wu, X. Wu, S. Xiao, G. Liu, and H. Li, Broadband wide-angle multilayer absorber based on a broadband omnidirectional optical Tamm state, Opt. Express **29,** 23976 (2021).

[11] S.-A. Biehs, C. Xu, and G. S. Agarwal, Strong coupling of collection of emitters on hyperbolic meta-material, J. Opt. **20,** 045601 (2018).

[12] D. J. Roth, A. V. Krasavin, A. Wade, W. Dickson, A. Murphy, S. Kéna-Cohen, R. Pollard, G. A. Wurtz, D. Richards, S. A. Maier, and A. V. Zayats, Spontaneous emission inside a hyperbolic metamaterial waveguide, ACS Photonics **4,** 2513 (2017).

[13] G. I. López-Morales, M. Li, R. K. Yadav, H. R. Kalluru, J. K. Basu, C. A. Meriles, and V. M. Menon, Spontaneous emission dynamics of Eu^{3+} ions coupled to hyperbolic metamaterials, Appl. Phys. Lett. **118,** 011106 (2021).

[14] C. Indukuri, R. K. Yadav, and J. K. Basu, Broadband room temperature strong coupling between quantum dots and metamaterials, Nanoscale **9,** 11418 (2017).

[15] K. F. Mak, C. Lee, J. Hone, J. Shan, and T. F. Heinz, Atomically Thin MoS_2: A New Direct-Gap Semiconductor, Phys. Rev. Lett. **105,** 136805 (2010).

[16] R. S. Sundaram, M. Engel, A. Lombardo, R. Krupke, A. C. Ferrari, P. Avouris, and M. Steiner, Electroluminescence in single layer MoS_2, Nano Lett. **13,** 1416 (2013).

[17] K. F. Mak, K. He, J. Shan, and T. F. Heinz, Control of valley polarization in monolayer MoS_2 by optical helicity, Nat. Nanotechnol. **7,** 494 (2012).

[18] H. Jiang, D. Ren, H. Wang, Y. Hu, S. Guo, H. Yuan, P. Hu, L. Zhang, and C. Li, 2D monolayer MoS_2–carbon interoverlapped superstructure: Engineering ideal atomic interface for lithium ion storage, Adv. Mater. **27,** 3687 (2015).

[19] W. Wu, L. Wang, Y. Li, F. Zhang, L. Lin, S. Niu, D. Chenet, X. Zhang, Y. Hao, T. F. Heinz, J. Hone, and Z. L. Wang, Piezoelectricity of single-atomic-layer MoS_2 for energy conversion and piezotronics, Nature **514,** 470 (2014).

[20] T. Mueller and E. Malic, Exciton physics and device application of two-dimensional transition metal dichalcogenide semiconductors, npj 2D Mater. Appl. **2,** 29 (2018).

[21] M. Y. Shalaginov, V. V. Vorobyov, J. Liu, M. Ferrera, A. V. Akimov, A. Lagutchev, A. N. Smolyaninov, V. V. Klimov, J. Irudayaraj, A. V. Kildishev, A. Boltasseva, and V. M. Shalaev, Enhancement of single-photon emission from nitrogen-vacancy centers with TiN/(Al, Sc)N hyperbolic metamaterial, Laser Photonics Rev. **9,** 120 (2015).

[22] A. Kala, F. A. Inam, S.-A. Biehs, P. Vaity, and V. G. Achanta, Hyperbolic metamaterial with quantum dots for enhanced emission and collection efficiencies, Adv. Opt. Mater. **8,** 2000368 (2020).

[23] J. A. Schuller, S. Karaveli, T. Schiros, K. He, S. Yang, I. Kymissis, J. Shan, and R. Zia, Orientation of luminescent excitons in layered nanomaterials, Nat. Nanotechnol. **8,** 271 (2013).

[24] S. Wang, Q. Le-Van, F. Vaianella, B. Maes, S. Eizagirre Barker, R. H. Godiksen, A. G. Curto, and J. Gomez Rivas, Limits to strong coupling of excitons in multilayer WS_2 with collective plasmonic resonances, ACS Photonics **6,** 286 (2019).

[25] G. Khitrova, H. M. Gibbs, M. Kira, S. W. Koch, and A. Scherer, Vacuum Rabi splitting in semiconductors, Nat. Phys. **2,** 81 (2006).

[26] D. G. Baranov, M. Wersäll, J. Cuadra, T. J. Antosiewicz, and T. Shegai, Novel nanostructures and materials for strong light–matter interactions, ACS Photonics **5,** 24 (2018).

[27] S. Wang, S. Li, T. Chervy, A. Shalabney, S. Azzini, E. Orgiu, J. A. Hutchison, C. Genet, P. Samorì, and T. W. Ebbesen, Coherent coupling of WS_2 monolayers with metallic photonic nanostructures at room temperature, Nano Lett. **16,** 4368 (2016).

[28] W. Liu, B. Lee, C. H. Naylor, H.-S. Ee, J. Park, A. T. C. Johnson, and R. Agarwal, Strong exciton–plasmon coupling in MoS_2 coupled with plasmonic lattice, Nano Lett. **16,** 1262 (2016).

[29] P. G. Sheasby and R. Pinner, *Surface Treatment and Finishing of Aluminum and its Alloys* (Finishing Publications Ltd. and ASM International, Materials Park, Ohio, 2001), 6th ed.

[30] R. K. Yadav, W. Liu, S. R. K. C. Indukuri, A. B. Vasista, G. V. P. Kumar, G. S. Agarwal, and J. K. Basu, Observation of photonic spin-momentum locking due to coupling of achiral metamaterials and quantum dots, J. Phys. Condens. Matter **33,** 015701 (2020).

[31] See Supplemental Material at http://link.aps.org/supplemental/10.1103/PhysRevApplied.18.014004 for sample fabrication procedure, raw spectral data, and additional details, which also includes references [58–68].

[32] P. Shekhar, J. Atkinson, and Z. Jacob, Hyperbolic metamaterials: Fundamentals and applications, Nano Converg. **1,** 14 (2014).

[33] H. N. S. Krishnamoorthy, Z. Jacob, E. Narimanov, I. Kretzschmar, and V. M. Menon, Topological transitions in metamaterials, Science **336,** 205 (2012).

[34] D. Y. Qiu, F. H. da Jornada, and S. G. Louie, Optical Spectrum of MoS$_2$: Many-Body Effects and Diversity of Exciton States, Phys. Rev. Lett. **111,** 216805 (2013).

[35] B. R. Carvalho, L. M. Malard, J. M. Alves, C. Fantini, and M. A. Pimenta, Symmetry-Dependent Exciton-Phonon Coupling in 2D and Bulk MoS$_2$ observed by Resonance Raman Scattering, Phys. Rev. Lett. **114,** 136403 (2015).

[36] Z. Jacob, I. I. Smolyaninov, and E. E. Narimanov, Broadband purcell effect: Radiative decay engineering with metamaterials, Appl. Phys. Lett. **100,** 181105 (2012).

[37] S. Li, P. Xu, and Y. Xu, Local photonic density of states in hyperbolic metasurfaces, J. Opt. **23,** 115101 (2021).

[38] R. C. Hilborn, Einstein coefficients, cross sections, f values, dipole moments, and all that, Am. J. Phys. **50,** 982 (1982).

[39] P. Törmä and W. L. Barnes, Strong coupling between surface plasmon polaritons and emitters: a review, Rep. Prog. Phys. **78,** 013901 (2014).

[40] G. Groenhof and J. J. Toppari, Coherent light harvesting through strong coupling to confined light, J. Phys. Chem. Lett. **9,** 4848 (2018).

[41] S. Sarkar, H. L. Pradeepa, G. Nayak, L. Marty, J. Renard, J. Coraux, N. Bendiab, V. Bouchiat, J. K. Basu, and A. Bid, Evolution of inter-layer coupling in artificially stacked bilayer MoS$_2$, Nanoscale Adv. **1,** 4398 (2019).

[42] H. L. Pradeepa, A. Bid, and J. K. Basu, Strong suppression of emission quenching in core quantum dots coupled to monolayer MoS$_2$, Nanoscale Adv. **2,** 3858 (2020).

[43] H. Leng, B. Szychowski, M.-C. Daniel, and M. Pelton, Strong coupling and induced transparency at room temperature with single quantum dots and gap plasmons, Nat. Commun. **9,** 4012 (2018).

[44] B. Peng, H. Zhang, H. Shao, Y. Xu, X. Zhang, and H. Zhu, Thermal conductivity of monolayer MoS$_2$, MoSe$_2$, and WS$_2$: Interplay of mass effect, interatomic bonding and anharmonicity, RSC Adv. **6,** 5767 (2016).

[45] T. Korn, S. Heydrich, M. Hirmer, J. Schmutzler, and C. Schüller, Low-temperature photocarrier dynamics in monolayer MoS$_2$, Appl. Phys. Lett. **99,** 102109 (2011).

[46] J. P. Reithmaier, G. Sek, L. A. C. Hofmann, S. Kuhn, S. Reitzenstein, L. V. Keldysh, V. D. Kulakovskii, T. L. Reinecke, and A. Forchel, Strong coupling in a single quantum dot–semiconductor microcavity system, Nature **432,** 197 (2004).

[47] Y.-J. Chen, J. D. Cain, T. K. Stanev, V. P. Dravid, and N. P. Stern, Valley-polarized exciton–polaritons in a monolayer semiconductor, Nat. Photon **11,** 431 (2017).

[48] J. B. Khurgin, How to deal with the loss in plasmonics and metamaterials, Nat. Nanotechnol. **10,** 2 (2015).

[49] T. Hümmer, F. J. García-Vidal, L. Martín-Moreno, and D. Zueco, Weak and strong coupling regimes in plasmonic QED, Phys. Rev. B **87,** 115419 (2013).

[50] M. Wersäll, J. Cuadra, T. J. Antosiewicz, S. Balci, and T. Shegai, Observation of mode splitting in photoluminescence of individual plasmonic nanoparticles strongly coupled to molecular excitons, Nano Lett. **17,** 551 (2017).

[51] D. S. Dovzhenko, S. V. Ryabchuk, Y. P. Rakovich, and I. R. Nabiev, Light–matter interaction in the strong coupling regime: configurations, conditions, and applications, Nanoscale **10,** 3589 (2018).

[52] L. Novotny, Strong coupling, energy splitting, and level crossings: A classical perspective, Am. J. Phys. **78,** 1199 (2010).

[53] M.-E. Kleemann, R. Chikkaraddy, E. M. Alexeev, D. Kos, C. Carnegie, W. Deacon, A. C. de Pury, C. Große, B. de Nijs, J. Mertens, A. I. Tartakovskii, and J. J. Baumberg, Strong-coupling of WSe$_2$ in ultra-compact plasmonic nanocavities at room temperature, Nat. Commun. **8,** 1296 (2017).

[54] Y. Sun, R. Wang, and K. Liu, Substrate induced changes in atomically thin 2-dimensional semiconductors: Fundamentals, engineering, and applications, Appl. Phys. Rev. **4,** 011301 (2017).

[55] H. Hogg, B.S thesis, Brigham Young University, Provo, UT, 2018.

[56] M. J. Shin, D. H. Kim, and D. Lim, Photoluminescence saturation and exciton decay dynamics in transition metal dichalcogenide monolayers, J. Korean. Phys. Soc. **65,** 2077 (2014).

[57] M. R. Gonçalves, H. Minassian, and A. Melikyan, Plasmonic resonators: fundamental properties and applications, J. Phys. D: Appl. Phys. **53,** 443002 (2020).

[58] E. E. Narimanov, H. Li, Y. A. Barnakov, T. U. Tumkur, and M. A. Noginov, Reduced reflection from roughened hyperbolic metamaterial, Opt. Express **21,** 14956 (2013).

[59] V. A. Podolskiy, A. K. Sarychev, E. E. Narimanov, and V. M. Shalaev, Resonant light interaction with plasmonic nanowire systems, J. Opt. **7,** S32 (2005).

[60] A. Castellanos-Gomez, M. Buscema, R. Molenaar, V. Singh, L. Janssen, H. S. J. van der Zant, and G. A. Steele, Deterministic transfer of two-dimensional materials by all-dry viscoelastic stamping, 2D Mater. **1,** 011002 (2014).

[61] J. D. E. McIntyre and D. E. Aspnes, Differential reflection spectroscopy of very thin surface films, Surf. Sci. **24,** 417 (1971).

[62] Y. Li, A. Chernikov, X. Zhang, A. Rigosi, H. M. Hill, A. M. van der Zande, D. A. Chenet, E.-M. Shih, J. Hone, and T. F. Heinz, Measurement of the optical dielectric function of monolayer transition-metal dichalcogenides: MoS$_2$, MoSe$_2$, WS$_2$ and WSe$_2$, Phys. Rev. B **90,** 205422 (2014).

[63] K. P. Dhakal, D. L. Duong, J. Lee, H. Nam, M. Kim, M. Kan, Y. H. Lee, and J. Kim, Confocal absorption spectral imaging of MoS$_2$: Optical transitions depending on the atomic thickness of intrinsic and chemically doped MoS$_2$, Nanoscale **6**, 13028 (2014).

[64] I. López Arbeloa and P. Ruiz Ojeda, Dimeric states of rhodamine B, Chem. Phys. Lett. **87**, 556 (1982).

[65] S. Tongay, J. Suh, C. Ataca, W. Fan, A. Luce, J. S. Kang, J. Liu, C. Ko, R. Raghunathanan, J. Zhou, F. Ogletree, J. Li, J. C. Grossman, and J. Wu, Defects activated photoluminescence in two-dimensional semiconductors: Interplay between bound, charged and free excitons, Sci. Rep. **3**, 2657 (2013).

[66] N. Saigal and S. Ghosh, Evidence for two distinct defect related luminescence features in monolayer MoS$_2$, Appl. Phys. Lett. **109**, 122105 (2016).

[67] I. I. Smolyaninov, *Hyperbolic Metamaterials* (Morgan and Claypool Publishers, San Rafael, 2018), 2053-2571.

[68] P. B. Johnson and R. W. Christy, Optical constants of the noble metals, Phys. Rev. B **6**, 4370 (1972).